Journal of Environmental Management 318 (2022) 115533

Contents lists available at ScienceDirect

Journal of Environmental Management

journal homepage: www.elsevier.com/locate/jenvman

Research article

# Synthesis of pozzolan and sugarcane bagasse derived geopolymer-biochar composites for methylene blue sequestration from aqueous medium

Hermann Tamaguelon Dzoujo [a,*], Victor O. Shikuku [b], Sylvain Tome [a], Saphan Akiri [c], Nadine M. Kengne [a], Soheil Abdpour [d], Christoph Janiak [d], Marie Annie Etoh [a], David Dina [a,**]

[a] Department of Chemistry, Faculty of Sciences, University of Douala, P.O. Box 24157, Douala, Cameroon
[b] Department of Physical Sciences, Kaimosi Friends University College, P.O. Box 385-50309, Kaimosi, Kenya
[c] School of Chemistry and Physics, University of KwaZulu-Natal, Private Bag X01, Scottsville, Pietermaritzburg, 3209, South Africa
[d] Institut für Anorganische Chemie und Strukturchemie, Universität Düsseldorf, Universitätsstr. 1, D-40225, Düsseldorf, Germany

ARTICLE INFO

*Keywords:*
Adsorption
Biochar
Geopolymers
Methylene blue
Pozzolan

ABSTRACT

In this study, four pozzolan-based geopolymers $GP_0$, $GP_5$, $GP_{10}$, and $GP_{20}$ were synthesized by alkaline activation and by substituting 0, 5, 10, and 20% of the precursor with sugarcane bagasse-derived biochar, respectively. The composites were characterized by X-ray fluorescence (XRF), X-ray diffraction (XRD), Fourier transform infrared spectroscopy (FTIR), scanning electron microscopy (SEM/EDX), and Brunauer–Emmett–Teller (BET) surface area analyses, and applied to sequester methylene blue (MB) dye in an aqueous medium in batch mode. The alkaline activation of pozzolan-biochar blends resulted in the formation of poly (Ferro-sialate-siloxo)-biochar chains. The adsorption capacity increased with an increase in biochar content from 24.44 to 455.46 mg/g (18-fold) for $GP_0$ and $GP_{10}$, respectively. The sorption kinetics of MB onto the composites followed pseudo-second-order kinetics while the equilibrium data were best described by the Sips isotherm model. The adsorption process was thermodynamically spontaneous, endothermic ($\Delta H = 14.32–32.20$ kJ/mol), and physical. The amount of adsorbent required for the removal of 99% of a fixed amount of MB in different volumes of effluent was predicted. Cost-analysis indicates that the composites are efficient and cheaper eco-adsorbents than commercial activated carbon and are suitable alternative candidates for the removal of dyes from water.

## 1. Introduction

Geopolymers are low cost and eco-friendly macromolecules resulting from a polycondensation/polymerization reaction between an amorphous aluminosilicate feedstock (fly ash, blast furnace slag, volcanic slag, silica fume, glass waste, red mud, etc.) and an activating solution (alkaline or phosphoric acid solution) at room or slightly elevated temperature ($T < 100\ ^\circ C$) (Davidovits, 1994; Tome Sylvain et al., 2019). They have an amorphous three-dimensional structure of zeolitic type (Zhang et al., 2008). The geopolymers thus developed have various domains of application in civil engineering, automotive industry, encapsulation of toxic waste, treatment of industrial effluents, etc. depending on their properties (Tome et al., 2018; Deventer et al., 2007; Victor Odhiambo and Tome Sylvain, 2019). Several previous works have shown the efficiency of geopolymers as adsorbents in the adsorption of methylene blue (MB) dye from aqueous media (Tome Sylvain et al., 2021; Hermann Dzoujo et al., 2021; El Alouani et al., 2019), since MB is known to cause adverse effects on the environment such as under-oxygenation, the proliferation of aquatic flora and inhibition of photosynthesis, among others (Fayoud et al., 2015). Fly ash, meta-kaolin, volcanic ash, and pozzolan are among the widely used precursors in the synthesis of these geopolymer adsorbents. However, the cost of thermal pretreatment and the unavailability of some industrial precursors can limit their use in many emerging economies relative to naturally occurring resources such as pozzolan. Furthermore, the geopolymerization products do not always guarantee materials with very high surface areas and high adsorption capacities (Bai and Colombo, 2018). In the quest to improve their textural properties and adsorption efficiencies, several adjuvants from mineral resources, agricultural wastes, and chemical additives have been reported. For example, the incorporation of Cetyl trimethylammonium bromide (CTAB) during synthesis improved the surface area, porosity, and copper

* Corresponding author.
** Corresponding author.
*E-mail addresses:* hermann.dzoujo@gmail.com (H.T. Dzoujo), dinadavidcr@yahoo.com (D. Dina).

https://doi.org/10.1016/j.jenvman.2022.115533
Received 19 March 2022; Received in revised form 1 June 2022; Accepted 12 June 2022

adsorption capacity of a metakaolin-based geopolymer (Singhal et al., 2017). The use of bivalent metallic ions ($Ni^{2+}$, $Zn^{2+}$, and $Ba^{2+}$) for chemical modification of slag-based geopolymer adsorbents have also been reported (Sarkar et al., 2018; Hanna et al., 2016). The use of hydrogen peroxide as an additive increased both the surface area and adsorption capacity of pozzolan-based geopolymer for the removal of MB (Hermann Dzoujo et al., 2021). These approaches, albeit useful, are not without limitations. The use of chemical adjuvants increases the overall cost of geopolymer development. The alternative is to evaluate the potential use of natural or waste materials. Shikuku Victor et al. (2021) reported the use of metakaolin (MK) to ameliorate the textural and MB adsorption characteristics of pozzolan-based geopolymer. The study revealed that though the addition of MK increased the geopolymer surface area, the adsorption capacity for MB was independent of the surface areas but rather controlled by the composition of the geopolymer. The surface area should, therefore, not be the sole criterion for the development and selection of adsorbents. The use of silica-rich agricultural waste, rice husk ash (RHA), was proposed by Barbosa and co-workers (Ramos et al., 2018). However, the role of the RHA fraction on the composition, textural properties, and adsorption dynamics of the developed geopolymers was not evaluated. Soybean oil was used as the additive rather than RHA. Therefore, the effect of agricultural waste chars on the adsorptive features of geopolymers needs to be examined as a synergistic means of waste management. Sugarcane bagasse (SCB) is an abundant, inexpensive, and promising type of industrial waste with a lignin-cellulose and polymer structure (50% cellulose, 25% hemicellulose, and 25% lignin) (Isabella Zanette da Silva et al., 2020). It is one of the precursors generally used in the preparation of activated carbons (ACs) and the resulting product has a large specific surface area and pore volume which is responsible for its good capacity to sequester pollutants. However, the preparation of AC is time-consuming and entails high production costs with relatively low yields per unit mass of feedstock due to the use of industrial chemicals and thermal treatment steps (≥500 °C) (Buapeth et al., 2019). Several works report the use of sugarcane bagasse ash as an additive in geopolymer mortars for the optimization of mechanical properties (Castaldelli et al., 2016; Buapeth et al., 2019). For example, partially replacing granulated blast furnace slag (GGBFS) with 10, 20, 30, and 40% sugarcane bagasse ash (SCBA) for the production of geopolymer concrete showed that the 20% SCBA fraction produced a geopolymer with a 22% higher strength than the 10% replacement and the control sample (Parthiban et al., 2020). The effect of sugarcane bagasse ash (SCBA) fractions on the compressive strength of blast furnace slag (BFS)-based geopolymers was reported by Castaldelli et al. (2013). These studies show that the effect of incorporation of biochars in geopolymer composites on the mechanical properties depends on the type of biomass, the biochar preparation conditions, the proportions of biochars added, and the geopolymer synthesis conditions. Though the agricultural waste chars have a remarkable impact on the physicomechanical properties of geopolymer mortars for construction purposes, to the best of our knowledge, no work to date describes the effects of biochar doses, and specifically SCB biochar, on the textural, compositional, and adsorption characteristics of geopolymers for the removal of dyes from water.

Considering the adsorbing properties of carbonized sugarcane bagasse in the literature (Shikuku Victor and Jemutai-kimosop, 2020), with added activation in alkali medium during geopolymer development, it is hypothesized that the incorporation of this alkali-activated agricultural waste (biochar) in pozzolan-based geopolymer would offer dual advantage of improved pollutant remediation capabilities and waste management.

This work aims to optimize the methylene blue (MB) dye adsorption performance of pozzolan-based geopolymers by incorporating carbonized sugarcane bagasse in the matrix to develop sustainable materials applicable in the treatment of industrial effluents. The effects of incorporating 0–20% of carbonized sugarcane bagasse on the textural, structural, composition, and adsorption characteristics for the removal of methylene blue from the aqueous phase under varying environmental conditions were examined and are herein reported.

## 2. Experimental method

### 2.1. Synthesis of geo-composites

The natural black pozzolan (previously dried, crushed, and sieved into particles smaller than 100 μm) that was used for the formulation of the eco-adsorbents was obtained from the Mbouroukou site (Latitude 4°; 45; 2.088″North; Longitude 9°; 38; 56.2088″East) while the sugarcane bagasse, used as an additive after pyrolysis, was collected in the city of Douala. These were dried, carbonized (between 150 °C and 350 °C) to improve the textural properties and amount of oxygen groups (Buapeth et al., 2019) for 1 h, ground, and sieved to a particle size of less than 100 μm.

The alkaline activator solution was prepared by mixing sodium hydroxide 12 M and sodium silicate. The sodium hydroxide and sodium silicate liquid to liquid ratio were 2.4. The geo-composites were formulated by substituting 0, 5, 10, and 20% of the pozzolan with carbonized sugarcane bagasse to improve the geopolymerization process and optimize the adsorbing properties of the resulting products. Alkaline solutions were added to the various precursor powders, with 0.3 liquid/solid ratios and the resulting pastes were left to rest for 30 min before moulding. These were then mechanically compacted for 1 min, oven-dried at 60 °C for 24 h, removed, then rested for 4 consecutive days. The resulting geo-composite samples, named $GP_0$, $GP_5$, $GP_{10}$, and $GP_{20}$, after immersion in acetone medium for 120 min for quenching the geopolymerization reaction, were oven-dried at 60 °C, crushed, sieved, washed to a neutral pH and again oven-dried for 6 h.

### 2.2. Materials characterization

The composition of different oxides present in pozzolan was determined by an x-ray fluorescence spectrometer (Bruker-SRS 3400). The ZEISS EVO L 15 scanning electron microscope (ESEM and EDX) operating at 20 kV accelerating voltage was used to carry out microscopic analyses while energy dispersive X-ray (EDX) analyses were carried out using an Oxford make EDX detector. The mineralogical composition of different materials was determined by X-ray diffraction (XRD). The diffractograms were obtained using an X-ray Powder Diffractometer (Bruker D8 Discovery, US) with the Bragg-Bretano theta-theta configuration in the 2θ range from 6° to 80° with a step of 0.02° and 1 s per step scan rate and CuKα radiation at 27.5 kV and 25 mA. The degree of crystallinity of the samples was computed as the ratio of the area of the crystalline peaks to the sum of areas of peaks for the amorphous and crystalline phases. The determination of the functional groups of feedstock, and geopolymer-composites before and after adsorption was achieved using Fourier Transform Infrared spectroscopy (FTIR). The infrared spectra were collected on Agilent Technologies, Cary 630 FTIR, and PerkinElmer Spectrometer 100. Nitrogen sorption isotherms for the determination of Brunauer-Emmett-Teller, BET surface areas were obtained at 77 K within a pressure range of $p = 10^{-3}$-1 bar on a Quantachrome Autosorb 6 (Quantachrome, Odelzhausen, Germany) instrument.

The pH drift method described by Karadag (Dogan, 2007) was used to determine the pH of the point of zero charge ($pH_{PZC}$). To 20 mL of 0.1 M NaCl solutions of pH between 2 and 12, 0.1 g of adsorbents were introduced and stirred kept at room temperature for 8 h after which the final pH values of the solutions were recorded with a pH meter (VOLTCRAFT PH-100ATC).

The procedures below described by Guèye (Sido-Pabyam et al., 2009) were used to determine the microporosity (iodine index) and macroporosity (methylene blue index) of the materials, respectively. For the Iodine Index, 0.1 g of composite material was oven-dried at 110 °C and added to 20 mL iodine solution (0.02 N) with continuous stirring for

5 min. A 0.1 N sodium thiosulfate solution was titrated with a 10 mL aliquot of the filtrate with starch as the color indicator. The determination of the Methylene blue Index was achieved by introducing 0.1 g of composite material into to 50 mL solution of methylene blue with continuous stirring for 5 min. The determination of the residual MB in the filtrate, measurements were done at a wavelength of 662 nm using a UV–visible spectrophotometer (MERCK spectroquant Pharo 300 UV/visible instruments).

### 2.3. Adsorption experiments

To study adsorption kinetic, 0.1 g of each adsorbent was added to a 50 mL of 50 mg/L MB solution and the mixtures were stirred at room temperature. At pre-determined time intervals, the residual methylene blue dye in the solution was determined. Equilibrium adsorption was studied at different initial methylene blue concentrations, where 0.1 g of sorbent was dispersed in 10–50 mg $L^{-1}$ of the sorbate in 50 mL solution, mixed at room temperature until equilibrium was achieved, and the concentration of MB in the supernatant liquid was determined. The quantities of MB fixed on the adsorbents at equilibrium ($q_e$) and the removal efficiency (%R) were calculated using Equations (1) and (2), respectively:

$$q_e = \frac{(C_i - C_e)V}{m} \quad (1)$$

$$R = \frac{(C_i - C_e)}{C_i} \times 100 \quad (2)$$

where $V$ is the volume of MB solution (L), $m$ is the mass of the sorbent (g), $C_i$ is the initial MB concentration and $C_e$ is the equilibrium MB concentration. The quantity of MB adsorbed at any given time ($t$) was obtained by Equation (3):

$$q_t = \frac{(C_i - C_e)V}{m} \quad (3)$$

### 2.4. Effect of temperature

A dose of 0.1 g of each adsorbent was introduced to 50 mL of MB solutions (50 mg $L^{-1}$). The mixtures were stirred at different temperatures (309, 319, 329, and 339 K) until the previously determined equilibration time.

### 2.5. Effect of pH

A 0.1 g of adsorbent was introduced to a 50 mL solution containing 50 mg $L^{-1}$ MB and agitated until equilibration. The pH of the initial solution was adjusted using 0.1 N HCl and 0.1 N NaOH solutions to a range of 2–12.

## 3. Results and discussion

### 3.1. Chemical and mineralogical analysis

Table 1. Shows the chemical composition of the different oxides present in the precursor pozzolan material and reported our previous work (Hermann Dzoujo et al., 2021). Composition-wise, the pozzolan tuff is a suitable material for the synthesis of geopolymers based on the aluminosilicate content (Davidovits, 2002).

Fig. 1 shows the diffractograms of the Pz precursor and carbonized

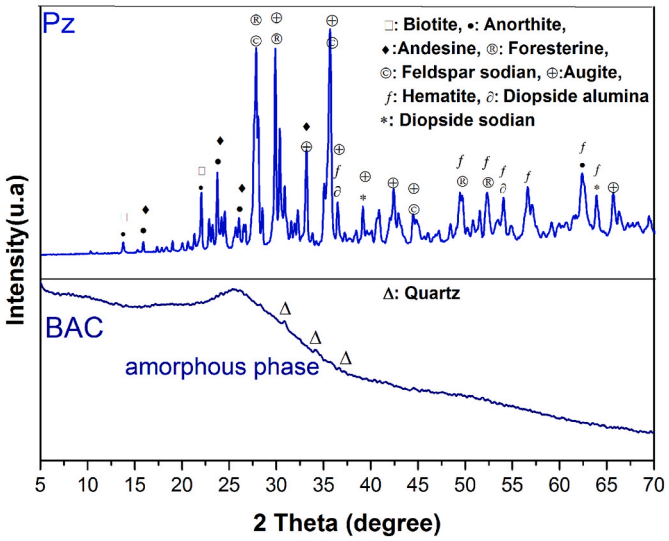


**Fig. 1.** XRD patterns Pz and BAC.

sugarcane bagasse. The precursor is made in anorthite (●), $Na(AlSi_3O_8)$ ($2\theta = 10.16°$, 13.72°, 15.86°, 21.97° and 25.93°) (PDF#01-073-6461), feldspar-Na (©), ($NaAlSi_3O_8$) ($2\theta$ = 27.65°,44.55° and 36.45°) (PDF#01-083-6911), forsterite (®), ($Mg_2SiO_4$) ($2\theta = 27.65°$, 49.53°and 53.93°) (PDF # 85–1462), diopside sodian (*), Ca(Mg, Fe, Al) (Si, Al)$_2O_6$ ($2\theta = 36.55°$ and 65.74°) (PDF#38–466), diopside alumina (a), Ca(Mg, Fe, Al) (Si,Al)$_2O_6$ ($2\theta = 36.45°$ and 53.93°) (PDF#38–0466), augite (⊕), ($Ca_{0.61}Mg_{0.76}Fe_{0.49}(SiO_3)_2$, ($2\theta = 33.18°$, 35.62°, 36.45°, 42.28°,44.55° and 65.74°) (PDF #76–0544), biotite (□), ($K(Mg,Fe)_3AlSi_3O_{10}(F,OH)_2$, ($2\theta$ = 10.16° and 21.97°) (PDF#01-080-1110), andesine (■),$Al_{1.488}Ca_{0.491}Na_{0.499}O_8Si_{2.506}$, ($2\theta = 13.72°$,15.86°, 25.93°, 27.65 and 33.18°) (PDF#01-079-1148) and hematite(*f*), $Fe_2O_3$ ($2\theta$ = 36.45°, 49.53°, 53.93°, 56.51°, 62.48° and 64.03°) (PDF#03–0812) as mineral phases. Moreover, the diffractogram of carbonized sugarcane bagasse shows a mostly amorphous phase with some traces of quartz, $SiO_2$ ($2\theta = 30.75°$, 34.29°, 36.58) (PDF#46–1045).

Fig. 2 shows the diffractograms of the geopolymer without ($GP_0$) and with the incorporation of carbonized sugarcane bagasse ($GP_{10}$), it is observed that the $GP_0$ geo-material presents the same mineralogical phases as the Pz precursor, reflecting a low dissolution of these phases during the geopolymerization. However, the crystallinity index of $GP_0$ (67.44%) being lower than that of the precursor (78.75%) indicates that amorphous gel formation occurred during polymerization. Furthermore, when comparing $GP_0$ and $GP_{10}$, the amorphous dome between 20 and 37° is observed, to be pronounced in $GP_{10}$, relative to $GP_0$, indicating a major transformation of the aluminosilicate phases with the incorporation of carbonized bagasse into the geopolymer network, as attested by the degree of crystallinity of 49.81% and 67.44% for $GP_{10}$ and $GP_0$, respectively. In addition to the appearance of this dome, it is also annotated with the presence of new crystalline phases such as moissanite (⊘), SiC (38.60°, 41.56°, and 42.70°) (PDF#00-001-1119), resulting from the reaction between silicon oxide and amorphous carbon of bagasse (Equation (4)) (Raman and Dhawan, 1995). Moreover, the decrease of the degree of crystallinity and the formation of the new crystalline phase with the incorporation of the carbonized bagasse are at the origin of the shift of the original phases (Table 2).

$$SiO_2 + 3C \rightarrow SiC + 2CO^{\uparrow} \quad (4)$$

**Table 1**
Bulk oxide composition of precursor.

| Oxides | $SiO_2$ | $Al_2O_3$ | CaO | $Fe_2O_3$ | $Na_2O$ | $K_2O$ | MgO | Cl | $SO_3$ | LOI |
|---|---|---|---|---|---|---|---|---|---|---|
| Pz (%) | 47.74 | 15.36 | 8.25 | 12.88 | 3.62 | 1.11 | 6.45 | - | - | 0.66 |

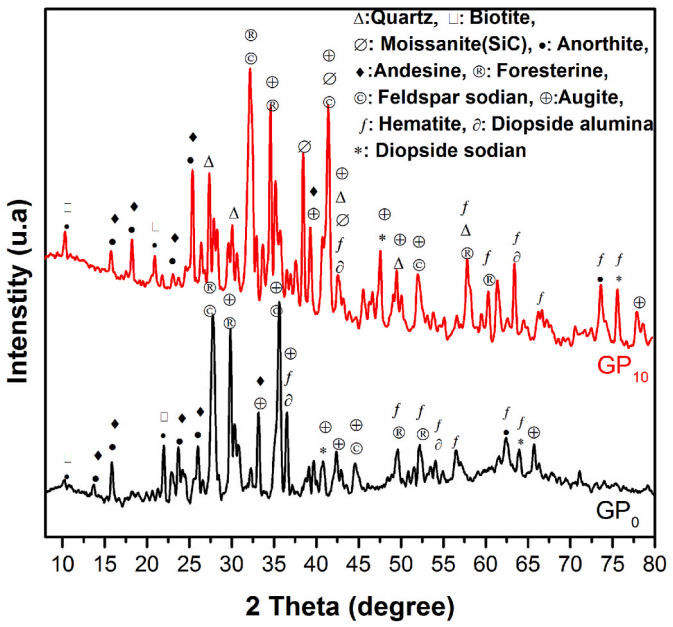


**Fig. 2.** XRD patterns of $GP_0$ and $GP_{10}$.

### 3.2. FTIR analysis

Fig. 3 shows the infrared spectra of carbonized and non-carbonized bagasse. The vibration bands observed around 3349 and 3318 $cm^{-1}$ correspond to the O–H stretching of the hydroxyl and carboxyl groups (Ahmed et al., 2021). This peak is less intense in the carbonized bagasse (BAC) spectrum probably due to the carbonization that would have evaporated some of the structural water contained in the plant material. The second band at 2933 and 2920 $cm^{-1}$ is attributable to aliphatic C–H stretching (Al-Mokhalelati et al., 2021). Those at 1619 and 1586 $cm^{-1}$ correspond to the stretching vibration resulting from carbonyls and C═C of aromatic bonds (Islam et al., 2017). The band at 1246 $cm^{-1}$ corresponds to the elongation vibration of the C–O bond in carboxylic acids, anhydrides, phenols, lactones, and ethers (Shen et al., 2018) and those observed around 1041 and 1030 $cm^{-1}$ correspond to the C–O stretching vibrations in ethers and esters. By comparing the spectrum of the BAC material with that of non-carbonized bagasse (BANC), a decrease in the intensity of the bands and disappearance of the characteristic peak of the C–O bonds located around 1246 $cm^{-1}$ after carbonization is observed, probably due to the decomposition of organic matter. As for the shift of the vibration bands from 3318, 2933, 1619, 1030 $cm^{-1}$ to 3349, 2920, 1586, and 1041 $cm^{-1}$ respectively, it reflects a graphitization of the structure (Al-Mokhalelati et al., 2021).

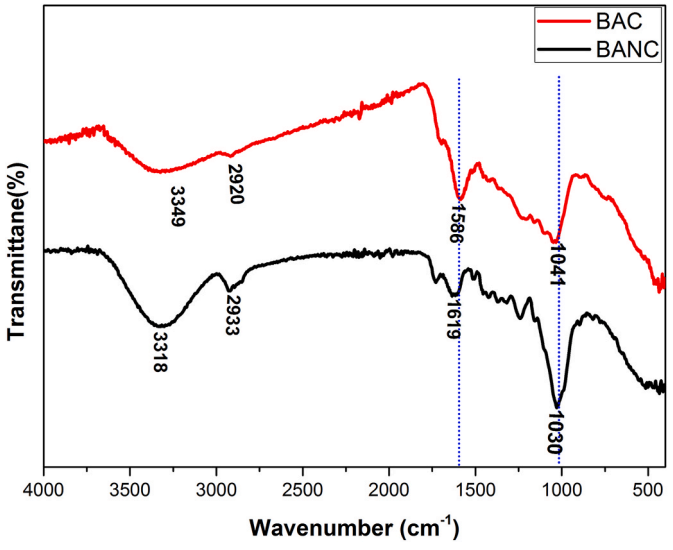


**Fig. 3.** FTIR spectra of carbonized (BAC) and non-carbonized (BANC) bagasse.

The FTIR spectra (Fig. 4) show the vibration bands of the different geopolymers.

The bands appearing in all the spectra in the regions between 3550 and 3400 $cm^{-1}$ and around 1650-1643 $cm^{-1}$ are attributed to the –OH stretching and H–O–H bending vibrations of the bound water molecules, respectively, that are adsorbed on the surface or trapped in the cavity of the geopolymer (Ioannis et al., 2009). The absorption bands around 1036-968 $cm^{-1}$ are attributable to the symmetric and asymmetric Si–O–Al or Si–O–Si elongation vibrations in the $SiO_4$ and $AlO_4$ tetrahedra of the geopolymer chain (Ramos et al., 2018). The band observed at 746 - 735 $cm^{-1}$ corresponds to the elongation vibration of the Si–O – Al bond. Finally, the band observed around 545-460 $cm^{-1}$ corresponds to the symmetrical elongation of Al–O–Al, Si–O–Fe, and Si–O–Si (Panias Dimitrios et al., 2007). Comparing the geopolymers obtained with and without the addition of carbonized sugarcane bagasse, it is observed that bands appear between 1464 and 1439 $cm^{-1}$ and at 847 $cm^{-1}$ within the geo-composites, respectively, attributable to the O–C–O vibrations of carbonates (Castaldelli et al., 2016) and Si–C vibrations of silicon carbide (Palizban and Ghasemian, 2016; Muthukumaran and Philip, 2020). On the other hand, the shift of the aluminosilicate peaks observed from 1036 to 995 $cm^{-1}$ denotes the reorganization of the aluminosilicate phases with the incorporation of the BACs. The presence of the Si–C vibration band, as well as the restructuring of the aluminosilicate phases, corroborate the results of XRD. Comparing the spectrum of the geocomposite before and after adsorption (Fig. 5), vibration bands at 1598, 1389, and 1325 $cm^{-1}$ are observed, attributable to the bending vibrations of methyl and methylene (Novais Rui et al., 2017), clear evidence of the fixation of MB on the geocomposite. Furthermore, the observed narrowing of the O–H (3395 $cm^{-1}$) and aluminosilicate (1005 $cm^{-1}$) elongation vibration bands is probably due to the exchange mechanism of $Na^+$ counter ions by $MB^+$ ions and other interactions

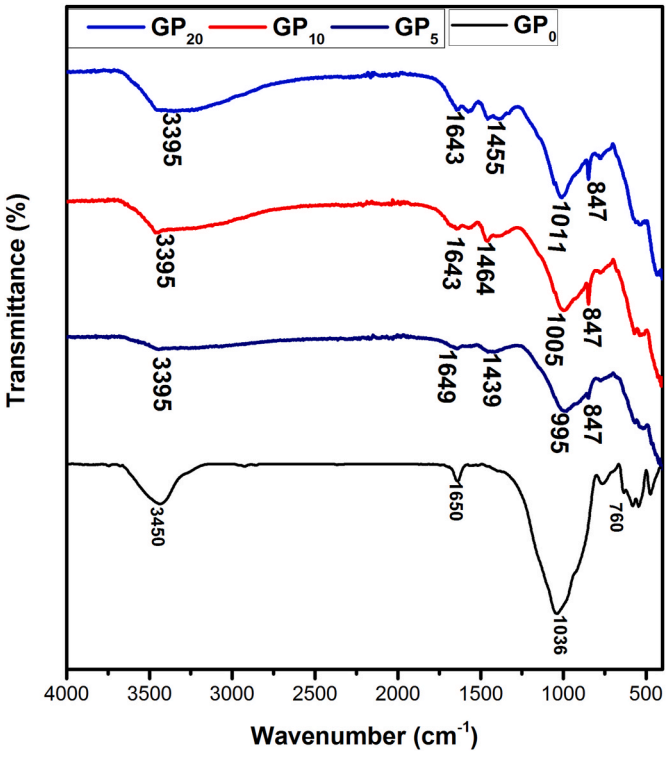


**Fig. 4.** FTIR spectra of the different geopolymers.

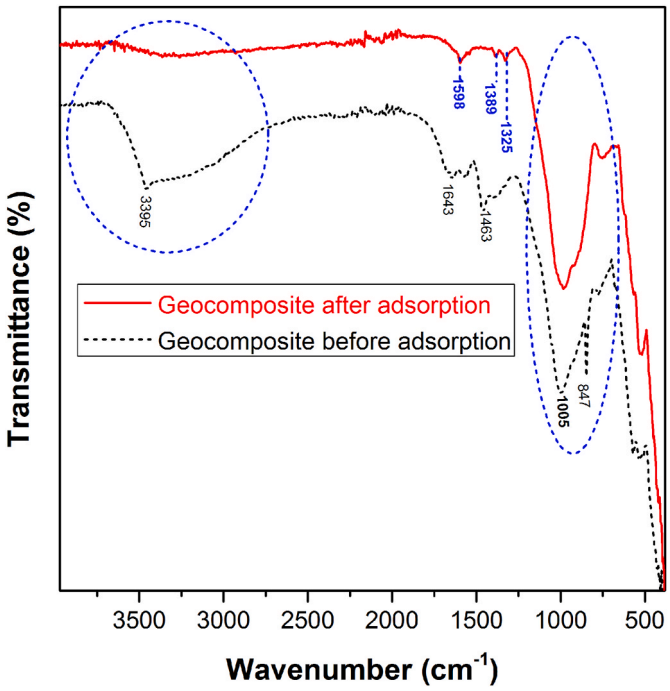


**Fig. 5.** FTIR spectrum of the geocomposite before and after adsorption of MB.

taking place in the geopolymeric network chain depicting the modification of the environment after adsorption.

### 3.3. SEM/EDX analysis

Fig. 6 represents the micrographs and the elemental composition of the precursors (Fig. 6a) and the selected samples of geopolymers without and with the incorporation of carbonized bagasse (Fig. 6b). From the pozzolan (Pz) microstructure, aggregates of crystallized aluminosilicate particles are observed, corroborating the XRD mineralogical analysis results. The micrograph of the carbonized bagasse (BAC) shows that it consists of homogeneous microporous and non-crystallized phases, the elemental analysis of these phases reveals that they are mainly composed of carbon and oxygen. However, the presence of potassium, calcium, silicon, and phosphorus in small proportions is also noted.

From the $GP_0$ microstructure, a densification of the aluminosilicate phases resulting from the polymerization/polycondensation reaction is observed. From previous works on the activation of volcanic slag in an alkaline medium, this macromolecule is a poly (Ferro-sialate-siloxo) chain (Jean Noel et al., 2016; Tome Sylvain et al., 2019). The $GP_{10}$ microstructure shows that the poly (ferro-sialate-siloxo) network and the biochar i.e. BAC form a homogeneous porous phase. Its EDX analysis reveals that there is an integration of carbon in the geopolymeric chain confirming the results of the XRD and FTIR analyses of this sample. The porous structure resulting from the poly (ferro-sialate-siloxo)-biochar combination has significantly better textural properties than the one without the biochar and could be a very efficient geo-adsorbent for MB adsorption.

### 3.4. Textural properties

Fig. 7 shows the iodine index and the methylene blue index of the different materials. It is observed that the different materials could have developed a higher microporosity due to the higher iodine index values (710.64, 444.15, 685.26, 634.50, and 329.94 mg/g for BAC, $GP_0$, $GP_5$, $GP_{10}$, and $GP_{20}$, respectively) than the methylene blue indices (24.40, 21.96, 17.45, 17.36, and 17.21 mg/g for BAC, $GP_0$, $GP_5$, $GP_{10}$, and $GP_{20}$, respectively). Taking into account the iodine values, the carbonized bagasse is more porous than the resulting geo-materials. The incorporation of BAC in the geopolymer matrix for a rate of 5%, increases the porosity. On the other hand, the incorporation of a rate higher than 5% decreases the porosity, attributed to the incorporation of a certain dose of carbonized plant matter that obstructs the pores of the geopolymers.

Table 3 presents the results of the BET analysis performed on the samples BAC, $GP_0$, $GP_{10}$, and $GP_{20}$. It is observed that the specific surface area and the total pore volume of the geopolymers increase with the increase of the biochar incorporation rate from 0 to 10% in the geopolymer matrix from 4.34 to 5.00 $m^2/g$ and 6.02 to 10 ( $\times 10^{-3}$ $cm^3/g$) for $GP_0$ and $GP_{10}$, respectively. Above 10%, the specific surface decreases from 5.00 to 3.00 $m^2/g$ for $GP_{20}$. These observations thus corroborate the discussions of iodine and methylene blue indices in the previous subsection. However, these changes were considered insignificant to distinguish the geopolymers.

### 3.5. Effect of pH

Figs. 8 and 9 show the pH at the point of zero charge (pHpzc) of the different materials and the evolution of the adsorbed amounts of MB as a function of the pH of the medium, respectively. Most of the materials have two zero charge points (Fig. 8), except for $GP_0$. The BAC material has a pHpzc of about 2 and 6.5 indicating that it has much more acidic functions (Buapeth et al., 2019) while those of the geocomposites ($GP_5$, $GP_{10}$, and $GP_{20}$) are about 2 and 7.5 indicating that these materials have basic and acidic groups contributed by the carbonized bagasse in the geopolymer matrix. This effectively shows that at pH < 5 for the geocomposites ($GP_5$, $GP_{10}$, and $GP_{20}$) and at pH < 7.5 for the $GP_0$ material (pH < pHpzc), the adsorption of MB is unfavorable due to electrostatic repulsions between the positively charged MB molecules and the surface of these positively charged adsorbents and the competition between the MB molecules and the $H^+$ ions, which, being more mobile, will reach the surface of the material more quickly than the MB molecules. This repulsion becomes less important when the quantity of $H^+$ ions is low in the medium of pH>5 for the geocomposites ($GP_5$, $GP_{10}$, and $GP_{20}$). In a basic environment, at pH > 7.5 (pH > pHpzc), adsorption is favorable due to the attraction between the MB and the negatively charged surface of the materials. Indeed, the hydroxide ions ($OH^-$) brought into the medium cause the deprotonation of the silanol (SiO–H) and aluminol (AlO–H) groups (El Alouani et al., 2019). The favorable adsorption of MB in acidic and basic media by geocomposites can also be justified by the increased number of binding sites.

### 3.6. Influence of contact time

Fig. 10 shows the change in MB adsorbed over time. At the onset of the reaction, a rapid increase in the adsorption process is exhibited, which stabilizes at around the 10th minute. After this phase, a slow and moderate adsorption phase is marked by desorption which extends from the 10th to the 30th minute on most materials suggesting pseudo-equilibrium conditions. Thereafter, there is an adsorption phase until equilibrium is reached, which is 10 min for BAC, 50 min for $GP_0$ and $GP_{10}$, and 60 min for $GP_5$ and $GP_{20}$. The fast kinetic at the beginning of the process is due to the availability of vacant active sites on the adsorbent, which leads to an increase in the adsorption rate. As for the desorption observed, it could be due to the detachment of the adsorbed molecules and adsorbate-adsorbate interactions. Fast kinetics imply a short residence time during water treatment.

### 3.7. Effect of initial MB concentration

Fig. 11 shows the amount and removal rate of MB adsorbed as a function of concentration. The amount of MB adsorbed increased linearly with the initial MB concentration since the flow of MB concentrations accelerates the diffusion and fixation process within the active sites

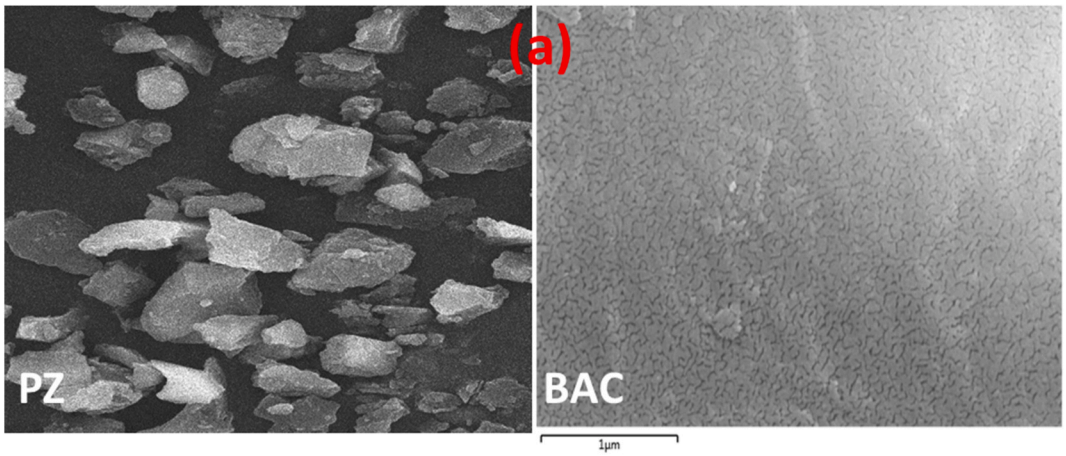


| Sample Pz | Wt% |
|---|---|
| Si | 15.11 |
| Al | 5.80 |
| Fe | 3.12 |
| Ca | 2.39 |
| Mg | 1.63 |
| Na | 1.46 |
| K | 0.38 |
| 0 | 43.71 |
| C | 0.01 |
| P | 0.02 |

| Sample BAC | Wt% |
|---|---|
| C | 75.54 |
| O | 21.93 |
| Na | 0.07 |
| Mg | 0.05 |
| Al | 0.06 |
| Si | 0.22 |
| P | 0.13 |
| S | 0.08 |
| K | 1.42 |
| Ca | 0.50 |

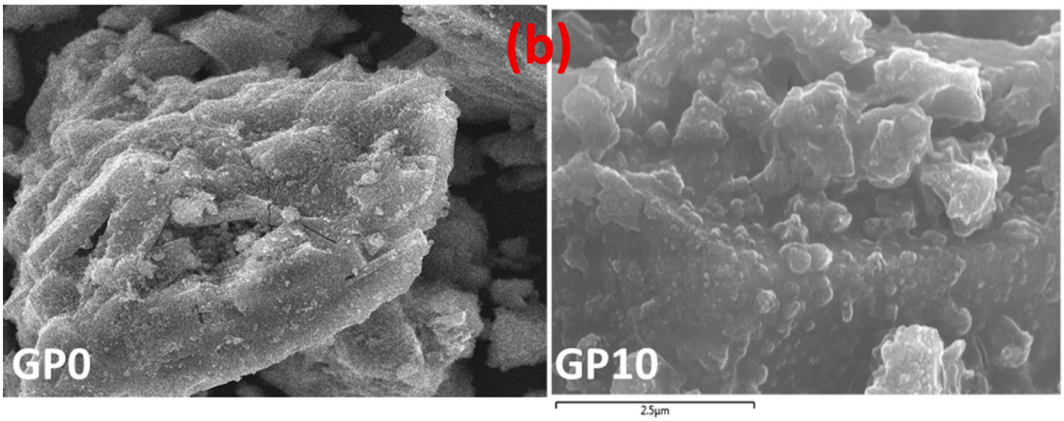


| Sample GP 0 | Wt% |
|---|---|
| Si | 15.91 |
| Al | 6.98 |
| Fe | 5.58 |
| Ca | 6.47 |
| Mg | 2.93 |
| Na | 2.82 |
| K | 0.52 |
| O | 45.17 |
| C | 0.01 |
| P | 0.00 |

| Sample GP 10 | Wt% |
|---|---|
| Si | 17.56 |
| Al | 4.35 |
| Fe | 5.58 |
| Ca | 8.33 |
| Mg | 4.43 |
| Na | 3.15 |
| K | 0.15 |
| O | 45.17 |
| C | 9.93 |
| P | 0.12 |

**Fig. 6. (a):** SEM image and EDX analysis of Pz and BAC **(b):** SEM image and EDX analysis of $GP_0$ and $GP_{10}$.

of different materials. In contrast to removal rates, a decrease in MB removal percentages is observed with increasing MB concentration. This is related to the difficulty of accessing the active sites by the MB molecules due to the repulsive forces between the MB molecules adsorbed on the surface of the materials and those in the solution.

### 3.8. Kinetics model

The kinetics data were modeled by non-linear regression of the pseudo-first-order (PFO) equation (5) (Ho and Mckay, 1998), and pseudo-second-order (PSO) equations (6) and (7) (Ho, 2006) and Vermeulen equation (8) (Yao and Chen, 2019). The experimental data were

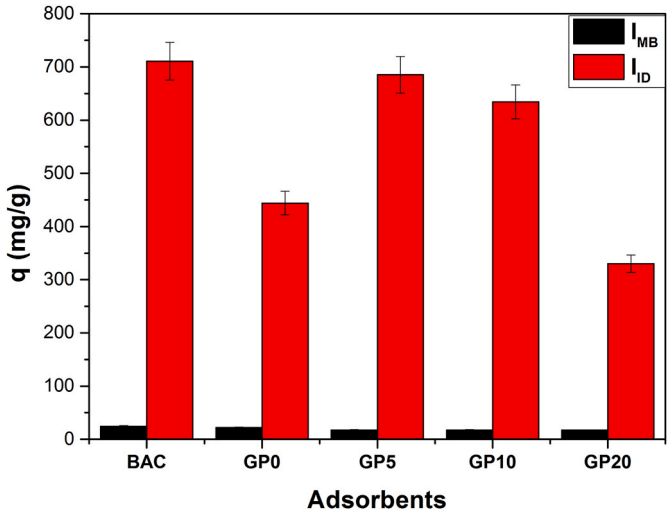


**Fig. 7.** Iodine ($I_I$) and methylene blue ($I_{MB}$) indices of the different materials.

**Table 3**
BET surface area and pores total volume of the samples.

| Sample | Pores total volume ( $\times 10^{-3}$ $cm^3/g$) | Surface area ($m^2/g$) |
|---|---|---|
| BAC | 10.00 | 8.00 |
| $GP_0$ | 6.02 | 4.34 |
| $GP_{10}$ | 10.00 | 5.00 |
| $GP_{20}$ | 10.00 | 3.00 |

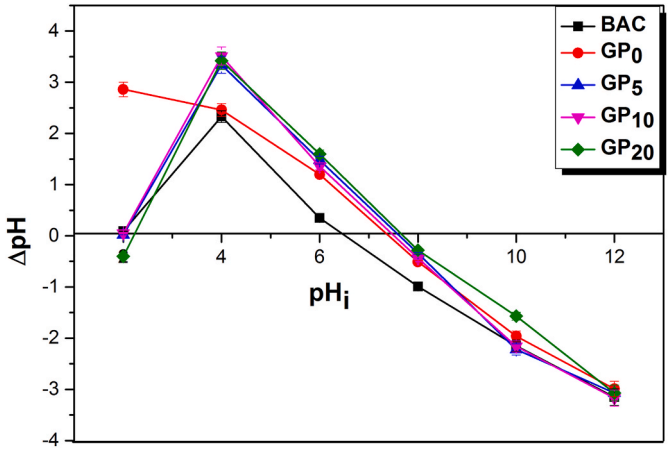


**Fig. 8.** Point of Zero Charge of materials.

compared with the predictions of the kinetic models to elucidate the mechanism controlling the adsorption kinetics of MB on the different eco-materials.**PFO:**

$$q = q_e\left(1 - e^{-k_1 t}\right) \tag{5}$$

where: q and $q_e$ are, respectively, the adsorbed quantities at instant *t* and equilibrium, $k_1$ ($min^{-1}$) is the Lagergren rate constant.**PSO:**

$$q = \frac{K_2 q_e^2 t}{1 + K_2 q_e t} \tag{6}$$

The half-life ($t_{1/2}$), as well as the initial rate of adsorption ($S_{rate}$), were determined by the relations below:

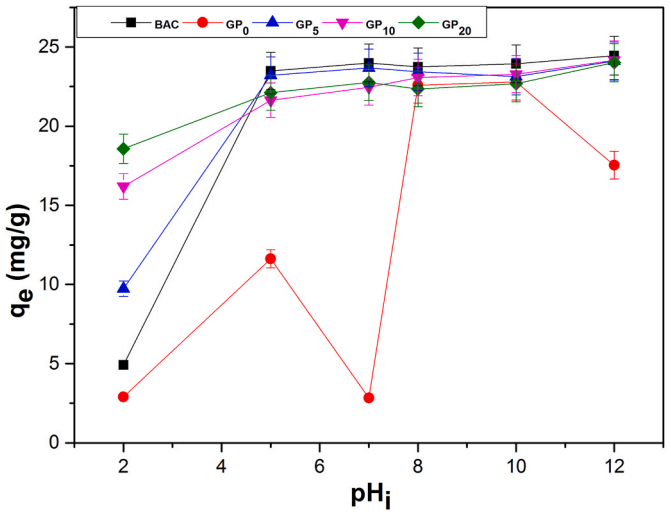


**Fig. 9.** Effect of pH on MB adsorption onto the different eco-adsorbents.

$$K_2 q_e = \frac{1}{t_{1/2}} \quad \text{With} \quad S_{rate} = k_2 q_e^2 \tag{7}$$

where: $t_{1/2}$ is the adsorption half-life, $K_2$ ($g.mg^{-1}.\ min^{-1}$) represents the PSO rate constant while $S_{rate}$ ($mg.g^{-1}.\ min^{-1}$) denotes initial sorption rate.**Vermeulen model**

$$q = q_e\sqrt{\left(1 - e^{-Bt}\right)} \tag{8}$$

where: B ($min^{-1}$) is the intraparticle diffusion constant.

From Table 4, the PSO kinetic model best described the kinetics of methylene blue fixation on the different materials (BAC, $GP_0$, $GP_5$, $GP_{10}$, and $GP_{20}$), relative to the pseudo-first-order and Vermeulen models, based on the coefficients of determination ($R^2$) closest to unity and the closeness between the values of the theoretically adsorbed quantities ($q_e$ (cal)) and those obtained experimentally ($q_e$ (exp)). This model also postulates a chemisorption mechanism of the rate-determining step (El Alouani et al., 2021). Moreover, the values of the rate constants ($K_2$) and initial MB adsorption rates ($S_{rate}$) decrease significantly for geo-adsorbents containing 0–10% biochar, reflecting a slow saturation of the active sites by MB molecules. Contrarily, the amount adsorbed at equilibrium increased with an increase in biochar content up to 10%.

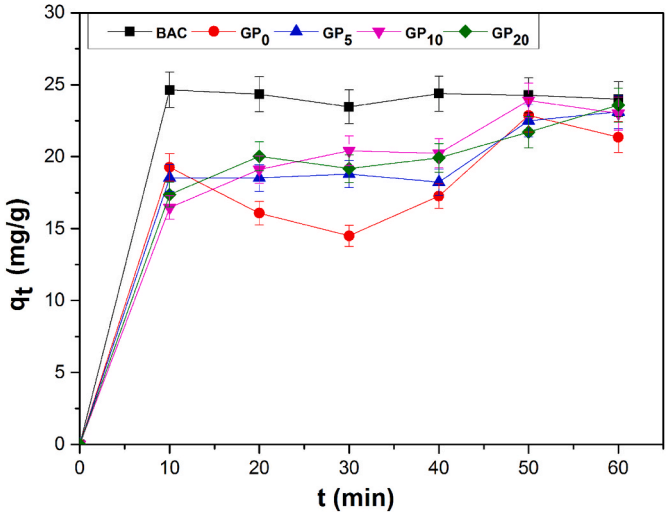


**Fig. 10.** Effect of contact time on the adsorption capacities of the different materials.

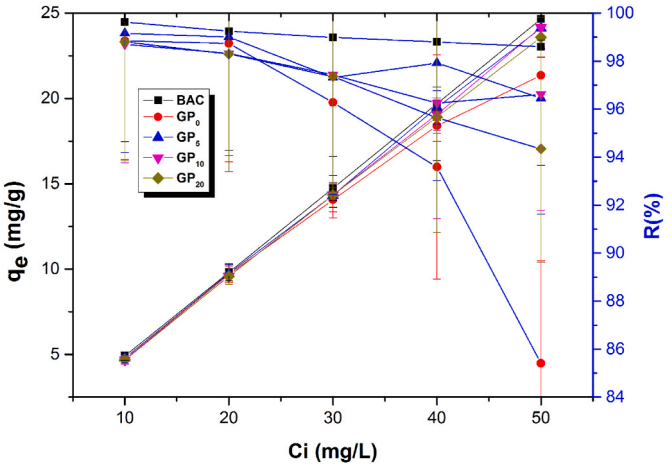


**Fig. 11.** Effect of initial MB concentration.

### 3.9. Adsorption isotherms

Five adsorption isotherm models (Langmuir, Freundlich, Temkin, Dubinin-Radushkevich-Kaganer, and Sips) were used to analyze the experimental equilibrium data and to predict the adsorption dynamics. The best-fitting model was determined using three error functions, *viz.* average relative error (ARE), the sum of absolute errors (EABS), and Chi-square ($\chi^2$) (Shikuku Victor and Mishra, 2021) shown in Table 5.

#### 3.9.1. Langmuir isotherm

The Langmuir isotherm (Irving, 1916) postulates monolayer adsorption of adsorbate onto a homogeneous adsorbing surface characterized by energetically identical binding sites.

$$q_e = \frac{Q_m K_L C_e}{1 + K_L C_e} \tag{9}$$

Where $q_e$ is the equilibrium dye concentration per unit mass adsorbent (mg $g^{-1}$), $C_e$ denotes equilibrium MB concentration in solution (mg $L^{-1}$), $Q_m$ is the theoretical monolayer maximum adsorption density (mg·$g^{-1}$) of the adsorbent whereas $K_L$ is the Langmuir constant (L $mg^{-1}$). Equation (10) was used to calculate the dimensionless separation factor, $R_L$ (Itodo, 2010). When $R_L$ lies in the range $0 < RL < 1$, the adsorption process is favorable, it is unfavorable when $R_L > 1$, linear when $R_L = 1$, and considered irreversible when $R_L = 0$(Ofomaja Augustine, 2008).

$$R_L = \frac{1}{1 + K_L C_0} \tag{10}$$

where: $C_o$ is the MB initial concentration.

#### 3.9.2. Freundlich isotherm

The Freundlich model (Freundlich, 1906) postulates a multilayer adsorption mechanism onto a heterogeneous surface. The Freundlich isotherm is expressed as Eq. (11):

$$q_e = K_F C_e^{1/n} \tag{11}$$

where $K_F$ represents the Freundlich constant (L $g^{-1}$) and $n$ is an exponential factor (dimensionless).

#### 3.9.3. Dubinin-radushkevich kaganer (D-R-K) isotherm

The D-R-K model (Eq. (12)) estimates the energy of adsorption and is useful in distinguishing between physisorption or chemisorption mechanisms (Itodo, 2010).

$$Q_e = Q_m \exp(-\beta \xi^2) \tag{12}$$

where $Q_e$ is the amount of MB in the solid phase at equilibrium (mg $g^{-1}$) and $Q_m$ is the theoretical maximum saturation density (mg $g^{-1}$) (Jia et al., 2013). The Polanyi potential ($\varepsilon$) is given by:

$$\xi = RT \ln\left(1 + \frac{1}{c_e}\right) \tag{13}$$

The mean adsorption energy $E_a$ (kJ/mol), given by eq. (14), distinguishes the physical from chemical adsorbent-adsorbate interactions.

$$E_a = \frac{1}{\sqrt{2\beta}} \tag{14}$$

#### 3.9.4. Temkin isotherm

The Temkin isotherm equation assumes that the heat of adsorption of all the molecules in the layer decreases linearly with coverage due to adsorbent– adsorbate interactions. The Temkin isotherm equation is given in Eq. (15) (Reyhaneh et al., 2015).

$$q_e = B_T \ln(A_T C_e) \tag{15}$$

where $B_T = RT/b_T$ is a constant related to the heat of adsorption (J/mol), $b_T$ represents the Temkin constant, and $A_T$ is the Temkin isotherm equilibrium binding constant (L/g). R is the universal gas constant (8.314 J/mol.K), and T (K) is the absolute temperature.

#### 3.9.5. Sips isotherm

The Sips model is a combination of the Freundlich and Langmuir isotherm equations. This model satisfactorily predicts adsorption onto the heterogeneous surfaces and monolayer adsorption assuming no adsorbate-adsorbate interactions. Equation (15) is an expression of the Sips isotherm model (Robert, 2004):

$$Q_e = \frac{Q_{ms} a_s C_e^{B_s}}{1 + a_s C_e^{B_s}} \tag{16}$$

**Table 4**
Calculated kinetics parameters.

| Models | Parameters | BAC | $GP_0$ | $GP_5$ | $GP_{10}$ | $GP_{20}$ |
|---|---|---|---|---|---|---|
| Pseudo first order | $K_1$ ($min^{-1}$) | 1.99 | 1.99 | 2.52 | 2.84 | 1.65 |
| | $q_e$ (cal) (mg $g^{-1}$) | 24.18 | 18.55 | 19.95 | 20.52 | 20.30 |
| | $q_e$ (exp) (mg $g^{-1}$) | 24.65 | 22.86 | 23.11 | 23.90 | 23.57 |
| | $R^2$ | 0.99 | 0.85 | 0.93 | 0.91 | 0.94 |
| Pseudo second order | $K_2$ (g $mg^{-1}min^{-1}$) | 29.05 | 0.04 | 0.02 | 0.01 | 0.01 |
| | $q_e$ (cal) (mg $g^{-1}$) | 24.19 | 19.52 | 21.948 | 24.81 | 23.11 |
| | $q_e$ (exp) (mg $g^{-1}$) | 24.65 | 22.86 | 23.11 | 23.90 | 23.59 |
| | $t_{1/2}$ (min) | 1.20 | 1.32 | 0.001 | 0.0003 | 0.0005 |
| | Srate (mg.$g^{-1}$.$min^{-1}$) | 16,997.09 | 14.84 | 8.52 | 4.46 | 6.41 |
| | $R^2$ | 0.99 | 0.86 | 0.95 | 0.98 | 0.98 |
| Vermeulen | B ($min^{-1}$) | 4.35 | 3.22 | 0.44 | 0.24 | 0.33 |
| | $q_e$ (cal) (mg $g^{-1}$) | 24.18 | 18.55 | 20.36 | 22.04 | 21.15 |
| | $q_e$ (exp) (mg $g^{-1}$) | 24.65 | 22.86 | 23.11 | 23.90 | 23.59 |
| | $R^2$ | 0.99 | 0.85 | 0.94 | 0.97 | 0.97 |

where $Q_{ms}$ (mg/g): is the sips maximum adsorption capacity, $a_s$ (L/mg): is the sips equilibrium constant and $B_s$ is the heterogeneity index.

Fig. 12 shows the non-linear isotherm plots of MB concentrations versus equilibrium adsorbed amounts on the different materials.

The suitability of the isotherms to predict the experimental data was determined by the coefficient of determination $R^2$ and the associated error function values (Table 6).

The Langmuir isotherm best described the adsorption of MB on the $GP_5$ material since the coefficient of determination is close to unity and the relatively low values of the error functions show a good fit between this model and the experimental data. In addition, the separation factor $R_L$ (0.03) being between 0 and 1 also indicates favorable adsorption of MB. This model thus reveals that the adsorption of MB on this geo-adsorbent takes place in a monolayer on the homogeneous active sites.

In terms of energetics, the acceptable representation of the equilibrium data by the Temkin model suggests that the heat of adsorption of all the molecules in the layer decreases linearly with the deposition of the adsorbate layer due to the decrease of adsorbate-adsorbent interactions and the adsorption process is characterized by a uniform distribution of binding energies on the surface (Reyhaneh et al., 2015).

The Sips isotherm best describes the MB attachment process on BAC, $GP_0$, and $GP_{10}$ materials since the error analysis values show that this isotherm modeled well the experimental data, unlike the other isotherms. The heterogeneity constant values (Bs > 1) of these adsorbents indicate highly heterogeneous systems due to the adsorbate-adsorbent interactions (Robert, 2004). The maximum adsorption capacities of MB on geo-composites predicted with the sips model show that the adsorbed uptake of MB increased from 24.44 to 455.46 mg/g for an incorporation rate of 0–10% of carbonized bagasse which could be attributed to an increase in energetically favored active sites numbers as revealed by the FTIR analysis. Beyond the 10% inclusion of carbonized bagasse, there is a decrease in the adsorption performances linked to

**Table 6**
Calculated isotherm parameters.

| Isotherms | Parameters | BAC | $GP_0$ | $GP_5$ | $GP_{10}$ | $GP_{20}$ |
|---|---|---|---|---|---|---|
| Langmuir | $Q_{max}$ (mg/g) | 46.04 | 23.90 | 36.82 | 124.83 | 67.66 |
| | $K_L$ (L/mg) | 0.74 | 0.92 | 0.66 | 0.10 | 0.18 |
| | $R_L$ | 0.03 | 0.02 | 0.03 | 0.17 | 0.10 |
| | $R^2$ | 0.84 | 0.92 | 0.83 | 0.95 | 0.97 |
| | $\chi^2$ | 2.11 | 2.86 | 3.87 | 1.89 | 1.01 |
| | EABS | 10.41 | 6.14 | 11.37 | 5.41 | 4.06 |
| | ARE | 13.30 | 19.14 | 23.60 | 14.83 | 11.63 |
| Freundlich | $K_F$(mg/g) (L/mg)$^1$ | 39.91 | 10.18 | 14.69 | 10.23 | 10.26 |
| | 1/n | 1.40 | 0.40 | 0.80 | 1.31 | 0.96 |
| | $R^2$ | 0.99 | 0.88 | 0.80 | 0.98 | 0.93 |
| | $\chi^2$ | 0.31 | 3.09 | 3.85 | 0.60 | 1.30 |
| | EABS | 2.71 | 9.11 | 13.44 | 4.81 | 8.40 |
| | ARE | 6.73 | 22.15 | 24.72 | 10.04 | 14.65 |
| D – R–K | $Q_{max}$ (mg/g) | 48.15 | 20.18 | 26.14 | 33.66 | 26.22 |
| | $E_a$ (KJ/mol) | 1.16 | 1.04 | 1.14 | 0.74 | 0.83 |
| | $R^2$ | 0.95 | 0.91 | 0.81 | 0.96 | 0.98 |
| | $\chi^2$ | 1.87 | 1.69 | 3.21 | 0.59 | 0.25 |
| | EABS | 6.27 | 8.08 | 13.33 | 6.21 | 3.93 |
| | ARE | 15.85 | 16.82 | 21.71 | 7.93 | 4.79 |
| Temkin | A (L/g) | 6.61 | 5.69 | 4.22 | 2.02 | 2.57 |
| | ΔQ (KJ/mol) | 14.05 | 5.95 | 11.08 | 16.62 | 11.58 |
| | $R^2$ | 0.89 | 0.93 | 0.82 | 0.96 | 0.99 |
| | $\chi^2$ | 2.48 | 1.75 | 3.08 | 0.49 | 0.13 |
| | EABS | 10.69 | 6.41 | 12.96 | 5.76 | 2.74 |
| | ARE | 20.13 | 16.39 | 21.35 | 7.29 | 4.46 |
| Sips | $Q_{ms}$ (mg/g) | 47,079.76 | 24.44 | 30.84 | 455.46 | 30.62 |
| | $a_s$ | 0.001 | 0.73 | 1.06 | 0.02 | 0.52 |
| | $B_S$ | 1.40 | 1.149 | 1.53 | 1.35 | 1.67 |
| | $R^2$ | 0.99 | 0.94 | 0.81 | 0.98 | 0.98 |
| | $\chi^2$ | 0.31 | 1.56 | 3.44 | 0.59 | 0.36 |
| | EABS | 2.71 | 5.54 | 13.62 | 4.79 | 4.11 |
| | ARE | 6.74 | 15.22 | 23.26 | 9.88 | 8.14 |

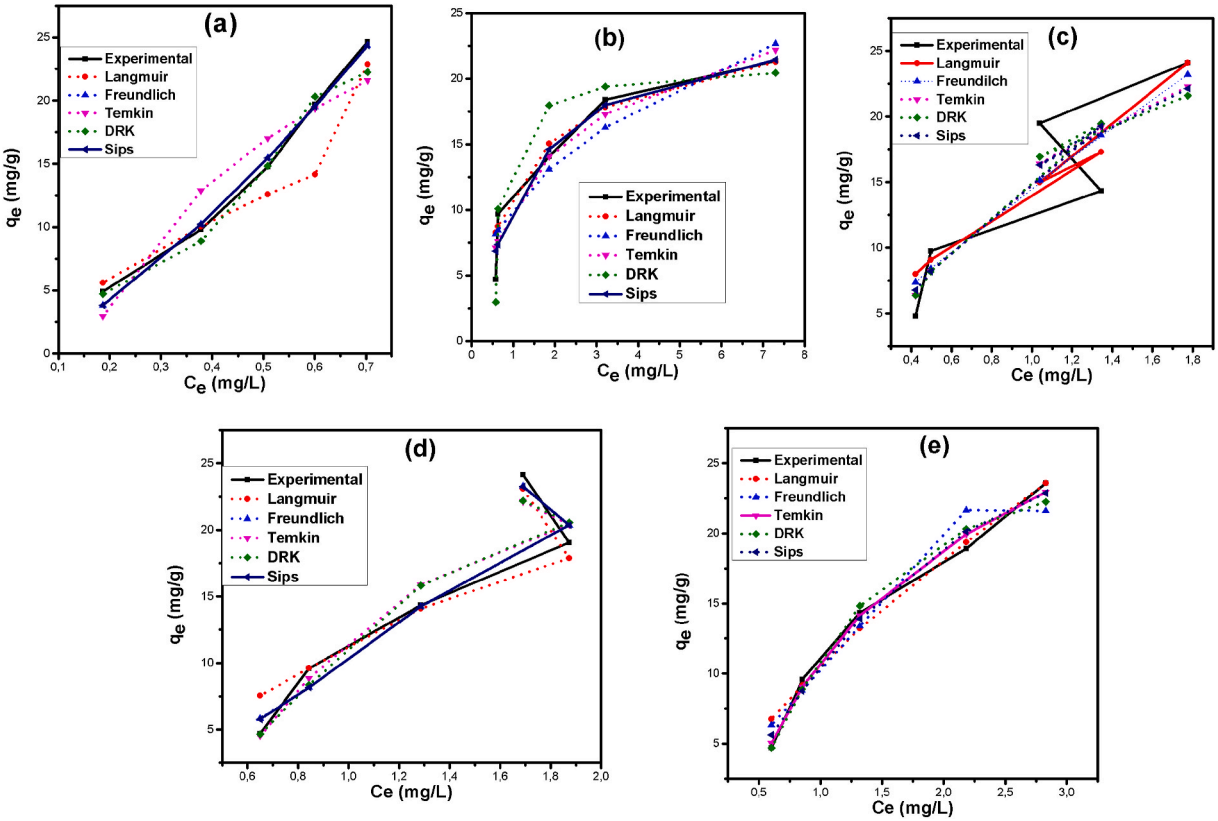


**Fig. 12.** Adsorption isotherm plots for MB onto (a) $GP_0$, (b) $GP_5$, (c) $GP_{10}$ and (d) $GP_{20}$ materials.

agglomeration resulting in inaccessible binding sites. This is because the materials seem to be identical in porosity. The adsorption capacity is therefore controlled by the geopolymer composition and not the textural properties. The values of the activation energies $E_a$ obtained from the D-R-K model were below 8 kJ/mol corresponding to a physisorption mechanism.

Table 7 highlights the comparison between MB retention capacities on the geopolymer-biochar composite and the various other adsorbents in the literature. The adsorption capacity of the $GP_{10}$ geocomposite was better than several reported in the literature and is potentially a suitable and efficient adsorbent for the retention of MB from water.

## 4. MB removal mechanism

The mechanism of MB attachment to the geopolymer-biochar is illustrated in Fig. 13. Considering the physicochemical characteristics of geocomposites discussed above, possible mechanisms associated with MB removal could be:

- Ions exchange between the MB cations and counterions ($Na^+$, $K^+$, $Ca^{2+}$and $Mg^{2+}$)
- Electrostatic interactions between the negative sites of geopolymers and positive sites of $MB^+$.
- π-π interactions between the carbon structure and the MB cycle structure.

### 4.1. Adsorption thermodynamics

In the temperature (T) range of 309–339 K, the effect of temperature on the adsorption thermodynamics functions of MB was investigated. Equations (17)–(20) were used for determining the three thermodynamic parameters, namely; enthalpy change (ΔH°), Gibb's free energy (ΔG°), and entropy (ΔS°), and the obtained values are presented in Table 8.

$$\Delta G^\circ = -RT \ln K_c \tag{17}$$

$$K_d = \frac{C_{ads}}{C_e} \tag{18}$$

$$K_c = 1000 K_d \tag{19}$$

$$\ln K_c = \frac{\Delta S^\circ}{R} - \frac{\Delta H^\circ}{R}\frac{1}{T} \tag{20}$$

where $K_c$ is the equilibrium constant (dimensionless), $C_e$ is the equilibrium MB concentration in the solution (mg $L^{-1}$) and $C_{ads}$ represents the equilibrium MB concentration in the solid phase (mg $g^{-1}$), $K_d$ is the distribution coefficient (L/g) and the density of water is 1000 g/L.

The negative values of ΔG° denote a spontaneous nature of the MB-composite adsorption process. The decrease in ΔG° values with an increase in temperature implies that the adsorption process is increasingly spontaneous a phenomenon consistent with an endothermic process. The low magnitudes of ΔG° values suggest a physisorption mechanism. The positive enthalpy (ΔH°) values confirm that the adsorption of the MB on the geo-adsorbents is an endothermic process. The positive values of entropy (ΔS°) indicate increased disorderliness at the solid/liquid interphase. Additionally, the ΔH° values, less than 40 kJ/mol, confirm that the adsorption of MB onto the geopolymer-biochar composites is a physical process (Shikuku Victor and Jemutai-kimosop, 2020), consistent with the ΔG° values and the postulates of the D-R-K model. The thermodynamics data indicate that the adsorption of MB onto the sorbents is entropy-driven.

**Table 8**
Thermodynamic parameters for MB removal by BAC, $GP_0$ and $GP_{10}$.

| Adsorbent | Temp. (K) | ΔG° (kJ $mol^{-1}$) | ΔH° (kJ $mol^{-1}$) | ΔS° (kJ $mol^{-1}$) |
|---|---|---|---|---|
| BAC | 309 | −20.10 | 7.37 | 0.09 |
| | 319 | −20.92 | | |
| | 329 | −21.83 | | |
| | 339 | −22.76 | | |
| $GP_0$ | 309 | −16.02 | 32.20 | 0.15 |
| | 319 | −16.66 | | |
| | 329 | −17.92 | | |
| | 339 | −20.84 | | |
| $GP_{10}$ | 309 | −22.63 | 14.32 | 0.12 |
| | 319 | −23.87 | | |
| | 329 | −25.01 | | |
| | 339 | −26.24 | | |

### 4.2. Adsorbent cost analysis

Adsorption isotherms are important tools in designing adsorption systems and for predicting the mass of $GP_{10}$ geoadsorbent, m (g), necessary for the removal of methylene blue in the effluent of volume V (L), from a known initial amount $C_i$ to an environmentally safe concentration $C_e$ (mg $L^{-1}$). This is important in the estimation of the cost-effectiveness of any adsorbent. Since the equilibrium data were best explained by the Sips isotherm, the amount of adsorbent required for given experimental conditions can be predicted by equation (21) (Shikuku Victor and Jemutai-kimosop, 2020).

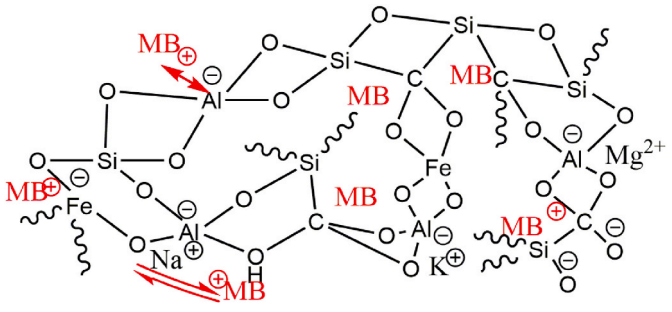


**Fig. 13.** Illustration of the different interactions between the geopolymer-biochar composite and MB.

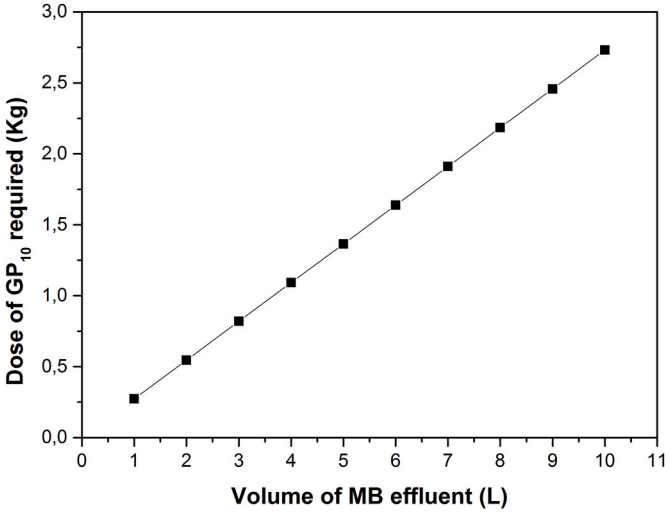


**Fig. 14.** Prediction of the amount of $GP_{10}$ required for the removal of MB in effluents of varying volume.

$$m = \frac{RC_i V\left(1 + a_s\left[C_i\left(1 - \frac{R}{100}\right)\right]^{B_s}\right)}{100 Q_{ms} a_s\left[C_i\left(1 - \frac{R}{100}\right)\right]^{B_s}} \quad (21)$$

Equation (21) was used to predict the mass $m$ (g) of $GP_{10}$ required for 99% sequestration of MB from effluents of different volumes (1–10 L) with an initial concentration of 50 mg $L^{-1}$ are results presented in Fig. 14. The values of the Sips isotherm constants are presented in Table 6.

From the plot, a dose of 2.73 kg of $GP_{10}$ is required to eliminate 99% of 50 mg $L^{-1}$ MB from a 10 L effluent. The cost of production of $GP_{10}$ was computed and compared with the market value of an equal amount of commercial activated carbon (CAC) in Cameroon (Table 9). The cost of production of GP was valued at about 2055.07 Euro cent/kg relative to the 23,076.93 Euro cent/kg price market for CAC. It is shown that the geopolymer in this work is 11 times cheaper than an equal amount of commercial activated carbon though the relative performance of the CAC is not herein reported. Nonetheless, it is conceivable that the geopolymers are efficient and techno-economical adsorbents for dye removal from water.

## 5. Conclusion

Four geopolymers $GP_0$, $GP_5$, $GP_{10}$, and $GP_{20}$ were synthesized *via* alkaline activation by substituting 0, 5, 10 and 20% of pozzolan with biochar derived from sugarcane bagasse and the products used to sorb cationic methylene blue (MB) dye from water. The incorporation of biochar before the geopolymerization process resulted in a poly (ferro-sialate-siloxo)-biochar chain. The incorporation of BAC biochar had an insignificant effect on the geopolymer textural properties. The adsorption capacity, controlled by geopolymer composition, increased from 24.44 to 455.46 mg/g when biochar content was increased from 0 to 10%, respectively. The sorption kinetics of MB onto the geopolymers followed the pseudo-second-order kinetics while the equilibrium data were best described by the Sips isotherm model. Thermodynamic studies reveal that adsorption is an endothermic and physical process. Cost-analysis demonstrates that geopolymer-biochar composites are efficient and cheaper adsorbents than commercial activated carbon.

## Credit author statement

David Dina, Sylvain Tome: Validation, Methodology, Writing - review & editing, Visualization, original draft. Dzoujo T. Hermann, Nadine M. Kengne, Saphan O. Akiri: Conceptualization, Methodology, Investigation, writing - original draft, resources. Victor O. Shikuku: Validation, Writing - review & editing. Saphan O. Akiri: Validation, Writing - review & editing. Marie-Annie Etoh: Writing - review & editing, Visualization. David Dina, Marie-Annie Etoh, Christoph Janiak, Victor O. Shikuku: Resources, Supervision.

## Declaration of competing interest

The authors declare that they have no known competing financial interests or personal relationships that could have appeared to influence the work reported in this paper.

## Acknowledgement

We thank the School of Chemistry and Physics in Scottsville (South Africa) and the Institute of Inorganic chemistry and structural in Dusseldorf (Germany) for providing analytical tools for materials characterization.

## Appendix A. Supplementary data

Supplementary data to this article can be found online at https://doi.org/10.1016/j.jenvman.2022.115533.

## References

Ahmed, Saud, Nadiah, Nurul, Firdaus, Mohd, Rangabhashiyam, S., Jawad, H., Lee, D Wilson, Mundher, Zaher, Al-kahtani, Abdullah A., Alothman, Zeid A., 2021. Journal of environmental chemical engineering statistical modeling and mechanistic pathway for methylene blue dye removal by high surface area and mesoporous grass-based activated carbon using K 2 CO 3 activator. J. Environ. Chem. Eng. 9 (4), 105530 https://doi.org/10.1016/j.jece.2021.105530.

Al-Mokhalelati, Kamal, Al-Bakri, Iman, Nesrin, Al Shibeh Al Wattar, 2021. Adsorption of methylene blue onto sugarcane bagasse-based adsorbent materials. J. Phys. Org. Chem. 2020, 1–9. https://doi.org/10.1002/poc.4193 no. November.

Bai, Chengying, Colombo, Paolo, 2018. Processing, properties and applications of highly porous geopolymers: a review. Ceram. Int. 44 (14), 16103–16118. https://doi.org/10.1016/j.ceramint.2018.05.219.

Buapeth, Preeyanit, Watcharin, Waralee, Dechtrirat, Decha, Chuenchom, Laemthong, 2019. Carbon adsorbents from sugarcane bagasse prepared through hydrothermal carbonization for adsorption of methylene blue : effect of heat treatment on adsorption efficiency carbon adsorbents from sugarcane bagasse prepared through hydrothermal carbonization. Mater. Sci. Eng. https://doi.org/10.1088/1757-899X/515/1/012003.

Castaldelli, Vinícius N., Akasaki, Jorge L., Melges, José L.P., Tashima, Mauro M., Soriano, Lourdes, Borrachero, María V., Monzó, José, Payá, Jordi, 2013. Use of slag/sugar cane bagasse ash (SCBA) blends in the production of alkali-activated materials. Materials 6, 3108–3127. https://doi.org/10.3390/ma6083108.

Castaldelli, V.N., Moraes, J.C.B., Akasaki, J.L., Melges, J.L.P., Monzó, J., Borrachero, M. V., Soriano, L., Payá, J., Tashima, M.M., 2016. Study of the binary system fly ash/sugarcane bagasse ash (FA/SCBA) in SiO 2/K 2 O alkali-activated binders. Fuel 174, 307–316. https://doi.org/10.1016/j.fuel.2016.02.020.

Davidovits, 1994. Geopolymers: man-made rock geosynthesis and the resulting development of very early high strength cement. J. Mater. Educ. 16, 91.

Davidovits, 2002. 30 Years of successes and failures in geopolymer applications . Market trends and potential breakthroughs. In: Geopolymer 2002 Conference . Saint-Quentin, vol. 28. Geopolymer Institute, Melbourne, Australia, pp. 1–16.

Deventer, J.S.J., van, Provis, J.L., Duxson, P., Lukey, G.C., 2007. Reaction mechanisms in the geopolymeric conversion of inorganic waste to useful products. J. Hazard Mater. 139 (3), 506–513. https://doi.org/10.1016/j.jhazmat.2006.02.044.

Dogan, Karadag, 2007. Modeling the mechanism , equilibrium and kinetics for the adsorption of acid orange 8 onto surfactant-modified clinoptilolite : the application of nonlinear regression analysis. Dyes Pigments 74. https://doi.org/10.1016/j.dyepig.2006.04.009.

El Alouani, Marouane, Alehyen, Saliha, El Achouri, Mohammed, Taibi, M'hamed, Mohammed, 2019. Preparation , characterization , and application of metakaolin-based geopolymer for removal of methylene blue from aqueous solution. Hindawi J. Chem. https://doi.org/10.1155/2019/4212901.

El Alouani, Marouane, Hamid, Saufi, Moutaoukil, Ghizlane, Alehyen, Saliha, Nematollahi, Behzad, Belmaghraoui, Walid, Taibi, M'hamed, 2021. Application of geopolymers for treatment of water contaminated with organic and inorganic pollutants : state-of-the-art review. J. Environ. Chem. Eng. 9 (2), 105095 https://doi.org/10.1016/j.jece.2021.105095.

Fayoud, N., Younssi, S Alami, Tahiri, S., Albizane, A., 2015. Etude Cinétique et Thermodynamique de l ' Adsorption de Bleu de Méthylène Sur Les Cendres de Bois (Kinetic and Thermodynamic Study of the Adsorption of Methylene Blue on Wood Ashes). J. Mater. Environ. Sci. 6 (11), 3295–3306.

Freundlich, Herbert, 1906. Über die adsorption in lösungen. Z. Phys. Chem. 57 (4), 385–470. https://doi.org/10.1515/zpch-1907-5723.

Hanna, Runtti, Tero, Luukkonen, Niskanen, Mikko, Tuomikoski, Sari, Kangas, Teija, Tynjälä, Pekka, , Emma-Tuulia Tolonen, Sarkkinen, Minna, Kemppainen, Kimmo, Rämö, Jaakko, Lassi, Ulla, 2016. Sulphate removal over barium-modified blast-furnace-slag geopolymer. J. Hazard Mater. https://doi.org/10.1016/j.jhazmat.2016.06.001.

Hermann Dzoujo, T., Tome, Sylvain, Victor, O Shikuku, Tchuigwa, Jean B., Alex Spieß, Janiak, Christoph, Etoh, Marie Annie, et al., 2021. Enhanced performance of hydrogen peroxide modified pozzolan-based geopolymer for abatement of methylene blue from aqueous medium. Silicon. https://doi.org/10.1007/s12633-021-01264-4.

Ho, Yuh-shan, 2006. Review of second-order models for adsorption systems. J. Hazard Mater. 136 (December 2005), 681–689. https://doi.org/10.1016/j.jhazmat.2005.12.043.

Ho, Y.S., Mckay, G., 1998. Sorption of dye from aqueous solution by peat. Chem. Eng. J. 70 https://doi.org/10.1016/S0923-0467(98)00076-1, 11.15-124.

Ioannis, Maragkos, Giannopoulou, Ioanna P., Panias, Dimitrios, 2009. Synthesis of ferronickel slag-based geopolymers synthesis of ferronickel slag-based geopolymers. Miner. Eng. 22, 196–203. https://doi.org/10.1016/j.mineng.2008.07.003. February 2018.

Irving, Langmuir, 1916. The constitution and fundamental properties of solids and liquids. J. Am. Chem. Soc. 38 (11), 2221–2295. https://doi.org/10.2121/ja02268a002.

Thaisa Caroline Andrade Siqueira, Isabella Zanette da Silva, Jenifer Rubio, Andressa, Bergamasco, Rosângela, Gasparotto, Francielli, Edneia Aparecida de Souza Paccola and Natália Ueda Yamaguchi, 2020. Sugarcane bagasse as an E ffi cient biosorbent for methylene blue removal : kinetics , isotherms and thermodynamics. Int. J. Environ. Res. Publ. Health Artic. 17, 526 https://doi.org/3390/ijerph17020526.

Islam, Azharul, Ahmed, M.J., Khanday, W.A., Asif, M., Hameed, B.H., 2017. Mesoporous activated coconut shell-derived hydrochar prepared via hydrothermal carbonization-NaOH activation for methylene blue adsorption. J. Environ. Manag. 203, 237–244. https://doi.org/10.1016/j.jenvman.2017.07.029.

Itodo, A.U., 2010. Sorption energies estimation using dubinin-radushkevich and. Life Sci. J. 7 (4), 68–76.

Jean Noel Yankwa, Djobo, Antoine, Elimbi, Sanjay, Kumar, 2016. Reactivity of Volcanic Ash in Alkaline Medium , Microstructural and Strength Characteristics of Resulting Geopolymers under Different Synthesis Conditions. J Mater Sci.

Jia, L.I.U., Wang, Hong-liang, Chun-xin, L.Ü., Han-fei, L.I.U., Zhi-xin, G.U.O., Kang, Chun-li, 2013. Water through modified diatomite. Chem. Res. Chin. Univ. 29, 3–6. https://doi.org/10.1007/s40242-013-2504-1, 2007.

Muthukumaran, T., Philip, John, 2020. A facile approach to synthesis of cobalt ferrite nanoparticles with a uniform ultrathin layer of silicon carbide for organic dye removal. J. Mol. Liq. 317, 114110 https://doi.org/10.1016/j.molliq.2020.114110.

Novais Rui, M., Ascensão, Guilherme, Tobaldi, David M., Seabra, Maria P., Labrincha, João A., 2017. Biomass fly ash geopolymer monoliths for effective methylene blue removal from wastewaters. J. Clean. Prod. https://doi.org/10.1016/j.jclepro.2017.10.078.

Ofomaja Augustine, E., 2008. Sorptive removal of methylene blue from aqueous solution using palm kernel fibre : effect of fibre dose. Biochem. Eng. J. 40, 8–18. https://doi.org/10.1016/j.bej.2007.11.028.

Palizban, E., Ghasemian, Z., 2016. Comparisons of azo dye adsorptions onto activated carbon and silicon carbide nanoparticles loaded on activated carbon. Int. J. Environ. Sci. Technol. 13 (2), 501–512. https://doi.org/10.1007/s13762-015-0875-1.

Panias Dimitrios, Giannopoulou, Ioanna P., Perraki, Theodora, 2007. Effect of Synthesis Parameters on the Mechanical Properties of Fly Ash-Based Geopolymers" 301: 246–54. https://doi.org/10.1016/j.colsurfa.2006.12.064.

Parthiban, Kathirvel, Gunasekaran, Murali, Sreekumaran, Sreenath, Krishna, Arathi, 2020. Effect of partial replacement of ground granulated blast furnace slag with sugarcane bagasse ash as source material in the production of geopolymer concrete. Mater. Sci. 26 (4), 477–481. https://doi.org/10.5755/j01.ms.26.4.23602.

Raman, BahlO., Dhawan, U.V., 1995. Synthesis of silicon carbide through the sol-gel process from different precursors. J. Mater. Sci. 30, 2686–2693. https://doi.org/10.1007/BF00362153.

Ramos, Barbosa Tuany, Luiz Foletto, Edson, Luiz Dotto, Guilherme, Luiz Jahn, Sérgio, 2018. Preparation of mesoporous geopolymer using metakaolin and rice husk ash as synthesis precursors and its use as potential adsorbent to remove organic dye from aqueous solutions. Ceram. Int. 44 (1), 416–423. https://doi.org/10.1016/j.ceramint.2017.09.193.

Reyhaneh, Saadi, Zahra, Saadi, Fazaeli, Reza, Elmi Fard, Narges, 2015. Monolayer and multilayer adsorption isotherm models for sorption from aqueous media monolayer and multilayer adsorption isotherm models for sorption. Kor. J. Chem. Eng. https://doi.org/10.1007/s11814-015-0053-7 no. May.

Robert, Sips, 2004. On the structure of a catalyst surface. J. Chem. Phys. 490 https://doi.org/10.1063/1.1746922. January 1948.

Sarkar, Chayan, Kumar Basu, Jayanta, Samanta, Amar Nath, 2018. Experimental and kinetic study of fluoride adsorption by Ni and Zn modified LD slag based geopolymer. Chem. Eng. Res. Des. 142, 165–175. https://doi.org/10.1016/j.cherd.2018.12.006.

Shen, Dong, Cheng, Wen, Adebajo, Moses O., Chen, Gui, Hua, Wei, 2018. Applied clay science adsorption of methylene blue from aqueous solution onto porous cellulose-derived carbon/montmorillonite nanocomposites. Appl. Clay Sci. 161 (September 2017), 256–264. https://doi.org/10.1016/j.clay.2018.02.017.

Shikuku Victor, O., Jemutai-kimosop, Selly, 2020. Efficient removal of sulfamethoxazole onto sugarcane bagasse-derived biochar : two and three-parameter isotherms , kinetics and thermodynamics. S. Afr. J. Chem. 111–19 https://doi.org/10.17159/0379-4350/2020/v73a16.

Shikuku Victor, O., Mishra, Trilochan, 2021. Adsorption isotherm modeling for methylene blue removal onto magnetic kaolinite clay : a comparison of two - parameter isotherms. Appl. Water Sci. 1–9. https://doi.org/10.1007/s13201-021-01440-2.

Shikuku Victor, O., Tome, Sylvain, Hermann, Dzoujo T., Tompsett, Geoffrey A., Timko, Michael T., 2021. Rapid Adsorption of Cationic Methylene Blue Dye onto Volcanic Ash - Metakaolin Based Geopolymers. Silicon, 0123456789. https://doi.org/10.1007/s12633-021-01637-9.

Sido-Pabyam, Guèye, Blin, Somé, 2009. Valorisation de Résidus de Biomasse En Charbons Actifs - Tests d'efficacité Sur Des Bactéries et Dérivés de Pesticides Biomass. Inernational Institute for Water and Environnemtal Engineering, pp. 65–73. https://www.2ie-edu.org/index.php?option=com_content&view=article&id=926&lang=fr.

Singhal, Aditi, Gangwar, Bhanu P., Gayathry, J.M., 2017. Applied clay science CTAB modi fi ed large surface area nanoporous geopolymer with high adsorption capacity for copper ion removal. Appl. Clay Sci. J. 150 (April), 106–114. https://doi.org/10.1016/j.clay.2017.09.013.

Tome, S., Etoh, M.-A., Etame, J., Sanjay, K., 2018. Characterization and leachability behaviour of geopolymer cement synthesised from municipal solid waste incinerator fly ash and volcanic ash blends. Recycling 3 (4). https://doi.org/10.3390/recycling3040050.

Tome Sylvain, Etoh, Marie-Annie, Etame, Jacques, Kumar, Sanjay, 2019. Improved reactivity of volcanic ash using municipal solid incinerator fly ash for alkali-activated cement synthesis. Waste Biomass Valorization 11 (6), 3035–3044. https://doi.org/10.1007/s12649-019-00604-1.

Tome Sylvain, Hermann, Dzoujo T., Victor, O Shikuku, Stephen, Otieno, 2021. Synthesis , characterization and application of acid and alkaline activated volcanic ash-based geopolymers for adsorptive remotion of cationic and anionic dyes from water. Ceram. Int. J. https://doi.org/10.1016/j.ceramint.2021.04.097 no. February: 1–9.

Victor Odhiambo, Shikuku, Tome Sylvain, 2019. Polymer nanocomposites for advanced engineering and military applications. In: Noureddine Ramdani. Application of Geopolymer Composites in Wastewater Treatment: Trends, Opportunities, and Challenges Victor. Copyright, Hershey PA, USA 17033. https://doi.org/10.4018/978-1-5225-7838-3.ch005. Global, IGI.

Yao, Chuncai, Chen, Tianjiao, 2019. An improved regression method for kinetics of adsorption from aqueous solutions. J. Water Proc. Eng. 31 (May), 100840 https://doi.org/10.1016/j.jwpe.2019.100840.

Zhang, Yunsheng, Wei, S.U.N., Zongjin, L.I., 2008. Infrared spectroscopy study of structural nature of geopolymeric products. J. Wuban Univ. Technol.-Mater. 23 (4), 522–527. https://doi.org/10.1007/s11595-007-4522-7.